Thermal Infrared Spectroscopy (7-14 µm) of Silicates under Simulated Mercury Daytime Surface Conditions and their Detection: Supporting MERTIS onboard the BepiColombo Mission

Indhu Varatharajan[1,2], Claudia Stangarone[1], Franziska D. H. Wilke[3], Alessandro Maturilli[1], Jörn Helbert[1], Harald Hiesinger[4], Iris Weber[4]

[1]Department of Planetary Laboratories, Institute of Planetary Research, German Aerospace Center (DLR), Berlin, Germany.

[2]Institute of Geological Sciences, Freie University (FU) Berlin, Germany.

[3]GFZ German Research Centre for Geosciences, Telegrafenberg, 14473 Potsdam, Germany.

[4]Institut für Planetologie, Westfälische Wilhelms-Universität Münster, Germany

Contact: indhu.varatharajan@dlr.de

Highlights

1. Spectral emissivity of powdered silicates (7-14 µm) under simulated Mercury Daytime conditions are studied.
2. Silicates show strong and distinct spectral features in thermal IR (7-14 µm) spectral region.
3. Christiansen Feature (CF) and Restrahland Band (RB1) of silicates varies with temperatures under vacuum.
4. CF vs RB1 plot can uniquely distinguish major silicate groups in the emissivity spectral region.

Abstract

To support the data analysis for the MErcury Radiometer and Thermal Infrared Imaging Spectrometer (MERTIS) instrument on the ESA-JAXA BepiColombo mission, we have measured the thermal infrared emissivity of finely grained silicates (<25 μm grain size) at different temperatures under vacuum to simulate the daytime conditions on the surface of Mercury. The silicates were selected to represent the mineralogy of Mercury as closely as possible (Helbert et al., 2007; Namur and Charlier, 2017; Vander Kaaden et al., 2017). The set includes one olivine (a Mg-rich forsterite), three pyroxenes (diopside, enstatite, and hypersthene), five feldspars (plagioclase group; anorthite, labradorite, andesine, oligoclase, and K-feldspar; microcline) and a feldspathoid (nepheline). The emissivity measurements for each mineral was carried out within the MERTIS spectral range of 7-14 μm with temperatures increasing from 100 °C up to 500 °C under vacuum (~0.1 mbar). The relationships between the spectral parameters such as the Christiansen Feature (CF) position, first Reststrahlen band (RB1) position, RB1 emissivity, and RB spectral contrast and temperature were investigated for all silicates. The study shows that the RB1 position shifts to longer wavelengths, RB1 emissivity decreases, and RB spectral contrast increases with increasing temperatures for all silicates studied. We apply the plot of CF vs RB1 as a tool to discriminate the major silicate groups such as feldspars, pyroxenes, and olivine, regardless of the temperatures at which they were measured. The CF vs RB1 plot can facilitate the first order discrimination of the mineralogy of Mercury's surface with MERTIS. Moreover, this approach can be more widely used to map the igneous surface mineralogy of silicate targets such as the Moon, Mars, and S-type asteroids in the 7-14 μm spectral region with remote sensing from orbit and ground-based telescope observations.

Keywords: Mercury, Silicates, Emissivity, Spectroscopy, Christiansen feature, Reststrahlen band

1. Introduction

The geochemistry suite onboard NASA's MErcury Surface, Space ENvironment, GEochemistry, and Ranging (MESSENGER) mission (2011-2015) revealed compositionally diverse surface materials, including evidence for a volatile-rich interior (preferably sulfides) (Besse et al., 2015; Blewett et al., 2011; Goudge et al., 2014; Namur and Charlier, 2017; Vander Kaaden et al., 2017; Vilas et al., 2016). However, in the wavelength range of the spectrometer suite onboard MESSENGER, the mineralogy could not be unambiguously determined due to nearly featureless spectra suggesting space-weathered Fe^{2+}-poor and Ti-poor crustal minerals/materials (Izenberg et al., 2014).

On October 20, 2018, ESA/JAXA's BepiColombo mission was successfully launched to Mercury. The MErcury Radiometer and Thermal Infrared Imaging Spectrometer (MERTIS) payload onboard the Mercury Planetary Orbiter (MPO) of BepiColombo will be the first thermal infrared (TIR) hyperspectral imager (7–14 μm) and radiometer (7–40 μm) ever to orbit Mercury. The goal is to map the global spectral emissivity and surface temperature of Mercury at a spatial resolution of ~500 m/pixel and ~2 km/pixel respectively (D'Amore et al., 2019; Helbert et al., 2010; Hiesinger et al., 2020; Hiesinger et al., 2010). Within the thermal infrared (TIR) spectral region (7-14 μm), silicates display characteristic spectral features regardless of the abundance of Fe and Ti in their structures (Helbert et al., 2013b). Therefore, MERTIS will provide spatially resolved information on compositions of various geological terrains, including hollows and pyroclastic deposits, as well as information on rock abundance, grain size, thermal inertia, and surface temperature (Helbert et al., 2010; Hiesinger et al., 2020; Hiesinger et al., 2010).

Until now, Mercury's surface has been studied with mid-infrared (MIR) spectroscopy only from ground-based telescope observations (e.g., (Cooper et al., 2002) and references within). In order to understand the mineral endmembers contributing to the observed MIR

spectra of Mercury, most of these earlier telescopic studies, except for (Sprague et al., 2009), used inverted reflectance measurements (1-reflectance; Kirchhoff's law) of samples measured at laboratory conditions at room temperature and ambient pressure.

Mercury is the second hottest planet in the Solar System with no atmosphere and with a rotational period of ~59 days, which is equal to 2/3 of its orbital period. This very slow rotation of the planet influences the length of one day which is equivalent to 176 Earth days. During one day on Mercury, the surface experiences extreme temperature fluctuations, ranging from a maximum of 450°C (daytime) to a minimum of -170°C (night time) (Krotikov and Shchuko, 1975). The change in temperature induces a variation in the minerals density on the surface of the planet, by changing bond distances and angles of the crystal structures (Christensen et al., 2000; Koike et al., 2003). A significant change in the vibrational behavior is therefore observed with temperature (Chihara et al., 2001; Ferrari et al., 2020; Ferrari et al., 2014; Helbert et al., 2013b; Koike et al., 2003; Koike et al., 2006; Maturilli et al., 2014; Reitze et al., 2017; Stangarone et al., 2017; Varatharajan et al., 2019). Consequently, using 1-R is insufficient for accurately interpreting telescopic spectra to determine their mineral endmembers.

Hence, to accurately decipher the mineralogy of Mercury's surface, it is necessary to investigate the spectral behavior of a wide range of Mercury analogues as a function of temperature, reproducing the extreme surface conditions. Before the arrival of MESSENGER, (Helbert et al., 2007) reported the first set of silicate groups that could be found on Mercury surface from the results of previous ground-based telescope observations, which included a) Mg-rich olivine (forsterite), b) pyroxenes (enstatite, diopside, and hypersthene), c) plagioclase feldspars (andesine, labradorite, oligoclase, anorthite), d) potassium feldspar (microcline), and e) feldspathoids (nepheline). After MESSENGER, the silicate mineralogy of Mercury was studied with two different approaches on the basis of geochemistry data, i.e., the analytical approach to derive the normative mineralogy (Vander Kaaden et al., 2017) and experimental

geochemistry (Namur and Charlier, 2017). Interestingly, the overall silicate mineralogy of Mercury suggested by these studies did not differ from the previously suggested silicates reported in (Helbert et al., 2007) based on ground based telescopic observations. There are studies on the spectral behavior of some silicates including pyroxenes (Ferrari et al., 2014), forsterites (Stangarone et al., 2017), and komatiites (Maturilli et al., 2014) under simulated daytime surface conditions of Mercury. However, so far, a complete thermal infrared spectral library of these silicates under simulated daytime surface conditions of Mercury is missing. Such a spectral library should significantly increase the accuracy of deconvolution model results of not only MERTIS but also of telescopic observations of Mercury (Varatharajan et al., 2018).

As Mercury's regolith is likely composed of very fine particles (Shevchenko, 2002), we investigated the thermal infrared (TIR) emissivity (7-14µm) for the above mentioned silicates measured for the fine grainsize (<25µm) at a spectral resolution of 4 cm^{-1}. For each sample, the TIR emissivity was measured at 100 °C, 200 °C, 300 °C, 400 °C, and 500 °C under vacuum (~0.1 mbar) to simulate the different daytime thermal conditions on Mercury's surface depending on time and latitude. The results on the temperature-dependent spectral behavior of these silicates will hence improve the direct detectability and understanding of the distribution, abundance, and nature of silicates on Mercury along with physical properties such as grain size, porosity, and thermal inertia. All spectral measurements were conducted at the Planetary Spectroscopy Laboratory (PSL) located at the DLR Institute of Planetary Research, Berlin (see Section 3).

2. Sample selection, preparation and characterization

For more than a decade, PSL has been collecting natural and synthetic Mercury analogue materials from various sources in preparation of MERTIS science data (Ferrari et al., 2020; Ferrari et al., 2014; Helbert and Maturilli, 2009; Helbert et al., 2007; Helbert et al., 2013b;

Maturilli et al., 2019; Stangarone et al., 2017; Varatharajan et al., 2019). Among them, the silicate minerals include a) olivine: forsterite, b) pyroxenes: enstatite, hypersthene, diopside, and c) plagioclase feldspar: anorthite, labradorite, andesine, oligoclase, d) K-feldspar: microcline, and e) feldspathoid: nepheline. These samples were powdered to varying grain sizes using a jaw crusher and a corundum mortar. Any impurities within the powdered samples were removed by further hand-picking during visual investigation (Helbert et al., 2007). For this study, we only used the grain size fraction at < 25 μm to mimic the fine-grained nature of Mercury's surface.

The chemical characterization of the silicate samples was determined by electron probe micro-analysis (EPMA) using a JEOL Hyperprobe JXA-8530F plus equipped with a thermal field-emission cathode and five wavelength-dispersive spectrometers at the GFZ in Potsdam. The operating conditions were 15 kV accelerating voltage, 20 nA beam current, and a 2 μm probe size for pyroxene and 10 μm for feldspar samples to avoid element migration of Na. To quantify elemental concentrations, certified standards were used for calibration such as albite (Si, Al, Na), microcline (K), diopside (Ca), and hematite (Fe) for feldspar analyses. Acquisition times on peak were 20 s to 10 s and half of that on each background. For pyroxene investigation, a diopside (Ca, Mg, Si), rhodonite (Mn), rutile (Ti), chromite (Cr), hematite (Fe) and albite (Al) was used for standardization. Acquisition times on peak were 10 s to 40 s. For all analyses only Kα-Lines were used. Data correction taking into account the interactions of incident electrons with the target, matrix absorption and fluorescence was done with the a $\varphi(\rho Z)$ correction scheme (Armstrong, 1995). The EPMA is advantageous for its high spatial resolution and the possibility of backscattered electron (BSE)-controlled spot analysis, thus avoiding or, at least, minimizing excitation of tiny inclusions. The chemical composition and oxide contents obtained are listed in Table 1 and Table 2. The chemical characterization of forsterite and enstatite is taken from (Stangarone, 2017). The studied pyroxenes (diopside, enstatite, and hypersthene) are further analysed for their crystal structures using x-ray diffraction (XRD)

analysis, and therefore characterising the pyroxenes to low-Ca ortho- (diopside, enstatite) and high-Ca clino- (hypersthene) pyroxenes. The powder XRD patterns were recorded in transmission mode using a fully automated STOE STADI P powder diffractometer (Cu–Kα1 radiation) equipped with a primary monochromator and a MYTHEN detector. The patterns were recorded in the range of $2\Theta = 5° – 125°$ using a step interval of 0.05° where 2θ is the angle between incident X-ray beam and reflected X-ray beam. The Cu X-ray tube was operated at 40 kV and 40 mA. Peak positions were calibrated externally using the National Bureau of Standards (NBS) silicon standard.

3. Methods

3.1 Spectroscopy facility

PSL operates three identical FTIR spectrometers (Bruker Vertex 80V) and each of them operates under various configurations to enable emissivity, reflectance, and transmission spectroscopy of various planetary analogue materials (Maturilli et al., 2018b). Fig. 1a shows the current laboratory setup at PSL where three spectrometers are named as Bruker A, B, and C. Among them, Bruker B is equipped with gold-coated mirrors optimized for measurements in near- to far-IR spectral range (1 - 100 μm) and is also attached to an external emissivity chamber. The emissivity chamber is fitted with a high efficiency induction heating system and temperature sensors (thermopiles) for tracking the temperatures of the samples during measurements. The chamber is also fitted with a webcam to monitor the surrounding environment during the measurements (Fig. 1b). The emissivity chamber is isolated from Bruker B by a shutter which allows independent operation of the spectrometer and the chamber under vacuum conditions (~0.1 mbar). This unique setup enables direct emissivity measurements of the silicates studied under controlled and simulated Mercury surface conditions, i.e., under vacuum and at varying temperatures (~100 °C–500 °C) (Ferrari et al.,

2014; Helbert and Maturilli, 2009; Helbert et al., 2013a; Maturilli et al., 2018a; Stangarone et al., 2017; Varatharajan et al., 2019).

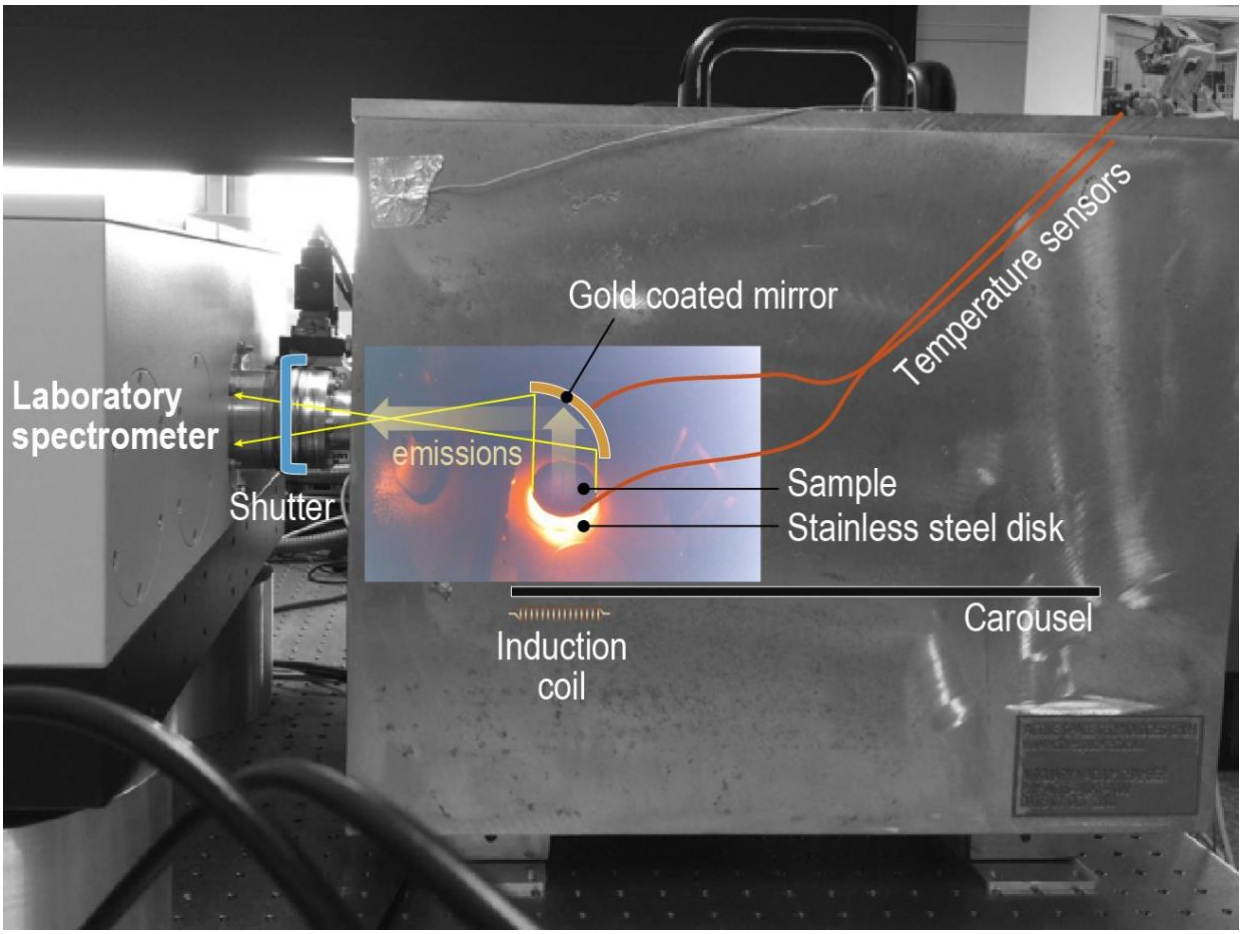

Figure 1. Graphical illustration of the laboratory set-up at PSL for high temperature emissivity measurements. The figure shows the heating of the sample cup using an induction coil and its corresponding emissions been deflected to the Bruker 80V spectrometer using a gold-coated mirror. The image from inside the chamber was taken by a webcam during the measurement. The samples are placed in a stainless-steel cup which is then placed on the carousel. The induction coil heats the sample cup through the carousel. The shutter between the spectrometer and emissivity chamber enables us to physically detach the emissivity chamber and spectrometer while heating under vacuum and therefore protecting the spectrometer from continuous heat emissions. The shutter is open only while recording the measurements when the sample cup reached its desired temperature.

Table 1. Summary of silicate minerals used in this study

Silicate Group	Mineral	Chemical composition*	Mineralogy	Locality
Olivines	Forsterite (Fo)	$Mg_{1.76}Fe_{0.22}X_{0.02}SiO_4$	Fo_{88}	San Carlos quality, Arizona
Pyroxenes	Diopside (Di)	$(Ca_1Mg_{0.9}Fe_{0.1})Si_2O_6$	$Wo_{50}En_{45}Fs_5$	Otter Lake, Quebec, Kanada (Krantz)
	Hypersthene (Hyp)	$(Mg_{1.4}Fe_{0.4}\ Ca_{0.2})_2Si_2O_6$	$Wo_{10}En_{70}Fs_{20}$	Egersund, Norwegen (Krantz)
	Enstatite (En)	$(Ca_{0.01}Mg_{1.73}Fe_{0.25}X_{0.01})Si_2O_6$	$Wo_{0.5}En_{86.5}Fs_{12.5}X_{0.5}$	Bamble, Norway
Plagioclase Feldspars	Anorthite (An)	$Ca_{0.95}Fe_{0.02}Al_{1.9}Si_{2.1}O_8$	$An_{95.5}Ab_{4.5}$	Insel Miyake, Tokio Bay, Miyakeshina, Japan
	Labradorite (Lab)	$Ca_{0.5}Na_{0.3}Al_{1.5}Si_{2.5}O_8$	$An_{51.2}Ab_{46.5}Or_{2.3}$	Madagaskar
	Andesine (Andes)	$Ca_{0.5}Na_{0.4}Al_{1.5}Si_{2.6}O_8$	$An_{47.4}Ab_{50}Or_{2.6}$	Saranac Lake, New York, USA (Krantz)
	Oligoclase (Olg)	$Ca_{0.3}Na_{0.6}Al_{1.2}Si_{2.8}O_8$	$An_{19.3}Ab_{76}Or_{4.7}$	Risör, Norwegen (Krantz)
K-Feldspar	Microcline (Mc)	$K_{0.6}Na_{0.4}AlSi_3O_8$	$An_{0.5}Ab_{31.9}Or_{67.6}$	Froland, Norwegen (Krantz)
Feldspathoid	Nepheline (Ne)	$Na_{0.75}K_{0.18}(Al_{0.95}SiO_4)$	$Neph_{100}$	Bancroft, Ontorio, Kanada (Krantz)

*chemical characterization of the minerals is listed in Table 2.

Table 2. Oxides content of the minerals listed in Table 1.

	Olivine	Pyroxene			Feldspar					Feldspathoid
wt%*	Fo	En	Di	Hyp	An	Lab	Andes	Olg	Mc	Ne
SiO_2	41.83	58.63	54.35	51.86	44.01	55.28	55.96	62.61	65.58	42.91
Al_2O_3	-	0.16	0.34	3.40	34.93	28.10	27.20	22.88	18.47	33.76
Na_2O	-	0.01			0.50	5.19	5.57	8.65	3.53	16.09
CaO	0.07	0.21	24.74	0.66	18.88	10.35	9.54	3.97	0.09	0.25
FeO	11.06	9.13	2.73	17.84	0.48	0.09	0.35	0.05	0.04	0.01
K2O	-	-	-	-	0.01	0.38	0.44	0.82	11.39	6.08
Cr_2O_3	0.03	0.01	0.01	0.06	-	-	-	-	-	-
TiO_2	0.03	0.05	0.04	0.20	-	-	-	-	-	-
MnO	0.17	0.04	0.15	0.29	-	-	-	-	-	-
MgO	48.97	34.06	16.44	24.51	-	-	-	-	-	-
Total	102.16	102.29	98.80	98.82	98.80	99.39	99.06	98.98	99.12	99.10

*Data in wt%. Forsterite and Enstatite composition is taken from (Stangarone, 2017)

3.2 Experimental set-up and procedure

The Bruker B is fitted with a MCT HgCdTe detector (cooled by liquid nitrogen) and a KBr beamsplitter, facilitating emissivity measurements in the spectral range of ~7-14µm (7–1400cm^{-1}) at a spectral resolution of 4 cm^{-1}. Each silicate sample (Table 1) is poured in a stainless-steel cup to a 3-mm-thick uniform layer. The cup is then placed on a carousel above the induction coil inside the external chamber (Fig. 1). Each cup is equipped with three thermopile temperature sensors; two of them measure the temperature of the emitting surface of the sample and the third one measures the temperature of the sample cup itself on its side. The experimental setup is shown in Fig. 1. The graphical flow chart of the measurement procedure is shown in Fig. 2 and is detailed below.

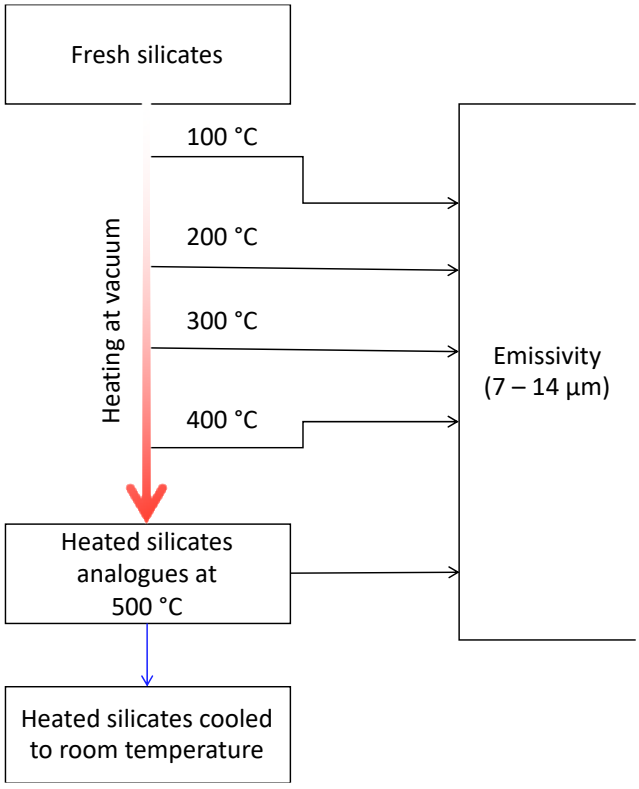

Figure 2. Graphical summary of the methodology used in the study to measure the temperature-dependent emissivity spectra.

a) The emissivity chamber and the Bruker B are slowly evacuated until they reach the desired vacuum (pressure of ~ 0.1 mbar).

b) After the instrument and chamber are stabilized at vacuum conditions and the cooled detector reaches a stable cold state, the sample is then slowly heated to ~100 °C by manually controlling the current to the induction system.

c) Once the sample surface temperature stabilizes at 100 °C, the emissivity measurement is initiated after opening the shutter between chamber and spectrometer. Thus, the radiance emitted from the heated silicate at ~100 °C is collected by a gold (Au) coated parabolic mirror with 90° off-axis, is then reflected into the spectrometer, and measured by the MCT detector. For each emissivity measurement, a set of 100 scans are obtained to increase the signal to noise ratio while maintaining the sample temperature stabilized at 100 °C by carefully controlling the current to the induction system.

d) After each measurement, the shutter is closed to avoid thermal instability of the Bruker instrument and the detector during the heating process.

e) This procedure is then repeated for emissivity measurements at 200 °C, 300 °C, 400 °C, and 500 °C by slowly increasing the current to the induction coil.

f) Over the entire heating period, the silicates are carefully monitored with the webcam installed in the chamber.

The thermally processed silicate sample is then cooled overnight down to room temperature in vacuum conditions. The entire procedure is repeated for every silicate sample listed in Table 1. All the measured emissivity spectra of silicates are then calibrated against a blackbody reference (in this case, blast furnace slag) for each measured temperature at the same geometric configuration (Maturilli et al., 2013). The calibrated sample emissivity of the silicates is shown in Fig. 3.

3.3 Spectral parameters studied

The three diagnostic spectral features in the TIR spectrum that are commonly used for remote identification and characterization of silicate minerals include the Christiansen feature (CF), Reststrahlen bands (RBs), and the transparency feature (TFs). The CF is an emissivity maximum that occurs near the Christiansen frequency where the real part of the refractive index of the sample approximately approaches the refractive index of the medium (in this study, the medium is vacuum) surrounding the mineral grains, and where the imaginary part of the refractive index is small (Conel, 1969; Hapke, 2012). The CF position (wavelength at emissivity maximum) is an index of silica polymerization and therefore the amount of Si-O; the CF position shifts to shorter wavelengths for highly polymerized silicates (Conel, 1969; Cooper et al., 2002; Donaldson Hanna et al., 2012; Logan et al., 1973). RBs relate to fundamental vibration bonds due to stretching and bending modes of Si-O and its cations, therefore RBs are used to identify the nature of the minerals such as olivines, pyroxenes, and feldspars (Conel, 1969; Hamilton, 2000; Lyon, 1965). TFs are the emissivity minima in the TIR spectrum caused by volume scattering of Si-O-Si bonds. TFs are more pronounced for small particle sizes (Cooper et al., 2002; Hapke, 2012).

In order to understand the nature of these diagnostic spectral features as a function of temperature, we derive following spectral parameters for all spectral measurements (Table S1 of supplementary material).

a) *CF position:* The wavelength position where the emissivity is at maximum shortward of the RB bands. The CF positions of the emissivity spectra of the silicates studied are marked as black arrows in Fig. 3.

b) *RB1 position*: The wavelength position where the first RB minimum longward of the CF position occurs. The RB1 positions of the emissivity spectra of the silicates studied are marked as red arrows in Fig. 3.

c) *RB1 emissivity:* The emissivity of the spectrum at the RB1 position.

d) *RB spectral contrast:* The difference between CF emissivity and RB1 emissivity is used to understand changes in spectral shape/band depth as a function of temperature.

e) TF position: The wavelength position where the first minimum longward of all RB bands occurs.

The emissivity maxima (CF) are derived by computing the maxima of the spectra within 7.5–9 μm spectral region. The RB1 position is computed by calculating the first band minima immediately after the CF position. Both minimum (RB1) and maximum (CF) values are derived by computing the minima and the maxima of the spectra within the given range due to the very high spectral resolution (4 cm^{-1}) of the measurements.

In addition to the derived spectral parameters, the corresponding minimum (min), maximum (max), average (avg), standard deviation, and Δμ (max-min) values were computed for the range of temperatures studied for each silicate. The derived spectral parameters and the computed statistics for all silicates are tabulated in Table S1 and are further discussed in the results section (Section 4).

4. Results

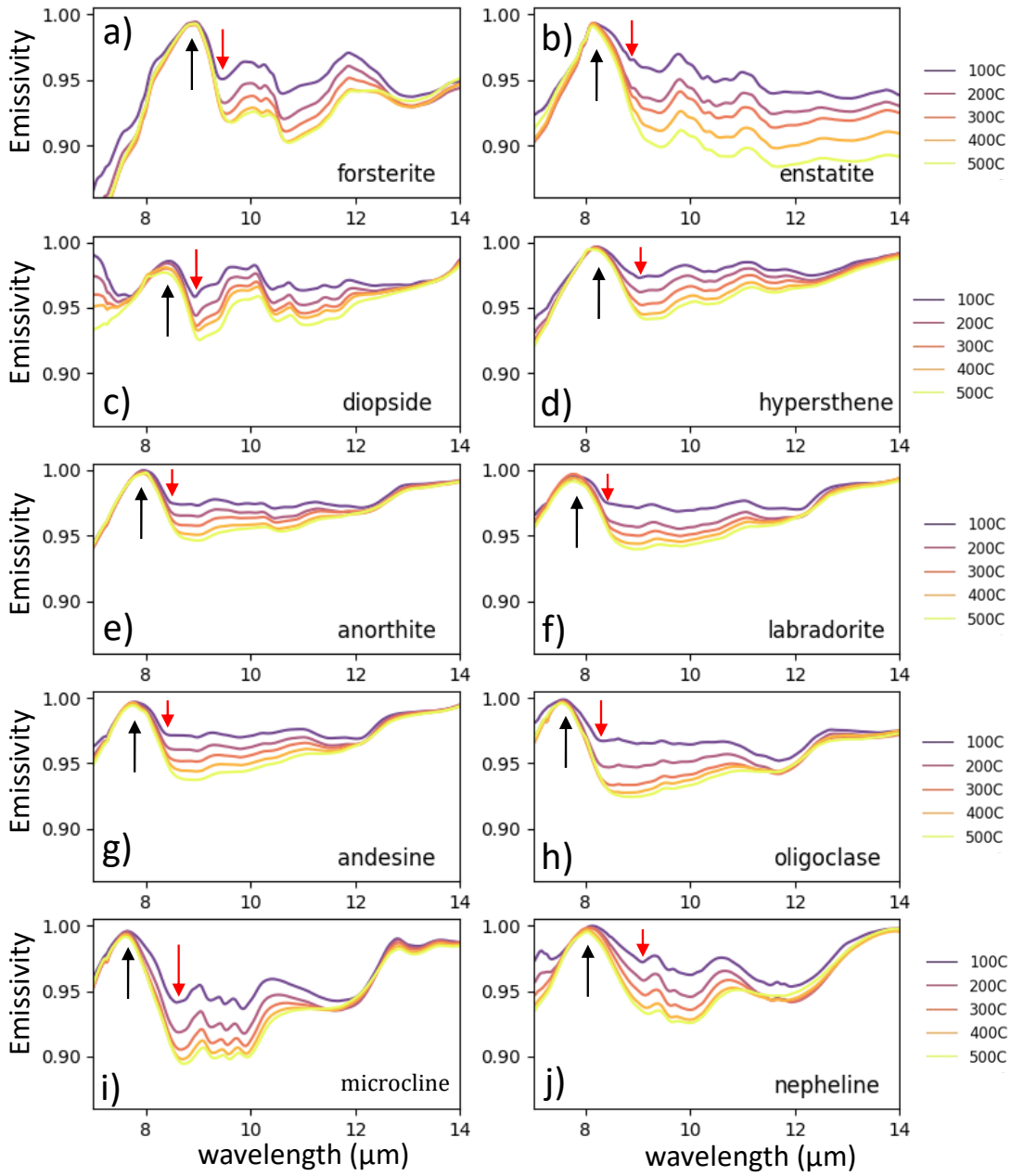

Figure 3. (a-j) Emissivity spectra of all the studied powdered silicates of grain sizes < 25 µm for temperatures 100 °C, 200 °C, 300 °C, 400 °C, and 500 °C under vacuum. Black arrows indicate the CF positions (emissivity maxima) for all silicates, and red arrows indicate the RB1 positions. The figure shows that for all silicates, the RB1 position shifts longwards with increasing temperatures and the RB1 emissivity decreases with increasing temperatures.

4.1. Olivine (forsterite)

The CF positions for the studied forsterite (Fo_{88}; Fig. 3a) are centered around ~ 8.93-8.95 μm and TF positions are located between 11.9 μm and 14 μm with the emissivity minimum centered around 13 μm at all temperatures under Mercury daytime surface conditions. The TF spectral contrast (difference between emissivity at 11.9 μm and 13 μm respectively) decreases with increasing emissivity. The RB1 position shifts longward from 9.45 μm to 9.64 μm with the increase in temperature. The RB spectral contrast increases with increasing temperature with $\Delta\mu$=0.032. Other RB bands between 9.45 μm and 12 μm include a minor RB at 8.4 μm and a major RB at 10.6 μm. The emissivity at these RBs decreases with the increase in temperature, similar to the emissivity of the RB1 position.

4.2. Pyroxenes (enstatite, diopside, hypersthene)

Enstatite ($Wo_{0.5}En_{86.5}Fs_{12.5}X_{0.5}$; Fig. 3b), diopside ($Wo_{50}En_{45}Fs_{5}$; Fig. 3c), and hypersthene ($Wo_{10}En_{70}Fs_{20}$; Fig. 3d) are the three pyroxenes studied for its emissivity behavior as a function of temperature. In the pyroxene quadrilateral diagram, enstatite is the Mg-endmember and hypersthene falls between the Mg-Fe join of pyroxene solid solutions (Morimoto, 1988), and both are orthopyroxenes. Diopside falls between the Mg-Ca join and is a clinopyroxene (Morimoto, 1988). For these pyroxenes, with increasing temperatures, CF positions shift shortwards ranging from 8.15-8.17 μm, 8.06-8.21 μm, and 8.35-8.43 μm for enstatites, hypersthene, and diopside, respectively. With increasing temperatures, the RB1 positions shift longwards with values ranging from 9.06-9.18 μm, 9.03-9.16 μm, and 8.94-9.03 μm, for enstatites, hypersthene, and diopside, respectively. The RB1 emissivity decreases with increasing temperatures. Thus, the RB1 spectral contrast increases with the increase in temperature for these pyroxenes with $\Delta\mu$ of 0.054, 0.030, and 0.024 for enstatites, hypersthene, and diopside, respectively.

Among these pyroxenes, diopside shows different behavior where the spectral slope between 7 μm and the CF position changes from positive to negative with increasing temperatures. The RB1 of diopside is the sharpest among the pyroxenes studied, accompanied by another minor band centered around 9.34 μm. Other minor bands centered around 10.4 μm, 11 μm, 11.63 μm can be spotted for diopside for all temperatures.

The RB1 of hypersthene is accompanied by a second broad RB centered around 10.43 μm. In enstatite spectra, the second broad RB contains minor triplet bands centered around 10.23 μm, 10.48 μm, and 10.76 μm.

The TF positions of the pyroxenes are not well pronounced as for other silicates (olivines, feldspars, and feldspathoid) studied, and therefore TF values for the pyroxenes are not derived and tabulated in Table S1.

4.3. Feldspars (anorthtite, labradorite, andesine, oligoclase, microcline)

The five feldspars studied, anorthite ($An_{95.5}Ab_{4.5}$; Fig. 3e), labradorite ($An_{51.2}Ab_{46.5}Or_{2.3}$; Fig. 3f), andesine ($An_{47.4}Ab_{50}Or_{2.6}$; Fig. 3g), and oligoclase ($An_{19.3}Ab_{76}Or_{4.7}$; Fig. 3h) belong to the plagioclase feldspar solid solution series between albite (Ab; $NaAlSi_3O_8$) and anorthite (An; $CaAl_2Si_2O_8$). Among the plagioclase feldspars studied in this solid solution series, the Ca content decreases going from: anorthite (95.5 mol% An) > labradorite (51.2 mol% An) > andesine (47.4 mol% An) > oligoclase (19.3 mol% An). In addition, the emissivity of microcline ($An_{0.5}Ab_{31.9}Or_{67.6}$), which belongs to the K-feldspar group and is commonly found in felsic volcanic rocks, was also studied (Fig. 3i) (Reitze et al., 2020).

Among the plagioclase feldspars (Fig. 3 e-h), the derived CF positions of the corresponding emissivity spectra for all temperatures shift shortwards with decreasing Ca contents in the order anorthite (7.94-8 μm) > labradorite (7.75-7.89 μm) > andesine (7.75-7.81 μm) > oligoclase (7.55-7.56 μm) in agreement with (Donaldson Hanna et al., 2012). Except for

anorthite, the CF positions for plagioclase feldspars shift shortwards with increasing temperatures. The CF position of anorthite slightly shifts longwards with increasing temperatures. Similar to CF positions, the derived RB1 positions show that for each plagioclase feldspar, the RB1 position shifts shortwards with decreasing Ca contents in the order: anorthite (8.47-8.68 μm) > labradorite (8.41-8.70 μm) > andesine (8.41-8.66 μm) > oligoclase (8.34-8.64 μm). For each plagioclase feldspar studied, the RB1 position shifts longwards and the RB1 emissivity decreases with increasing temperatures. Similar to the CF and RB1 positions, the RB1 spectral contrast of the plagioclase feldspars also show a correlation with their respective Ca contents. This behavior can be explained by the increase in Δμ of the RB spectral contrast with decreasing Ca contents; anorthite (0.025), labradorite (0.028), andesine (0.030), and oligoclase (0.039). The RB1 spectral contrast also increases with increasing temperatures. The RBs among the plagioclase feldspars are broad and weak and therefore the distinct RB minima are difficult to derive for these powdered silicates. The TF bands for these plagioclase feldspars center around 12.1 μm except for oligoclase spectra which have the TF band center at around 11.7 μm. However, for all the plagioclase feldspars, the TF band strength decreases with increasing temperatures (Fig. 3 e-h).

The emissivity spectra of the K-feldspar microcline (Fig. 3i) show a characteristically different spectral behavior compared to the plagioclase feldspars (Fig. 3 e-h) with pronounced RB bands centered around 8.6 μm, 9.2 μm, 9.5 μm, and 9.8 μm. The CF position and RB1 position of microcline range from 7.61-7.65 μm and 8.6-8.73 μm, respectively. With the increase in temperature, the CF position shifts shortwards and the RB1 position shifts longwards. The RB1 emissivity decreases with increasing temperatures leading to an increase in RB1 spectral contrast with Δμ of 0.043. The TF positions of microcline at all temperatures are centered around 11.7 μm, which is further accompanied by a minor broad absorption band near 13.1 μm, which shifts shortwards with increasing temperatures.

4.4 Feldspathoid (nepheline)

Nepheline is a silica-undersaturated alkaline aluminosilicate belonging to the feldspathoid family (Deer et al., 2013). The CF positions of emissivity spectra of nepheline ($Neph_{100}$; Fig. 3j) are centered around 8.03-8.13 μm for all temperatures. For nepheline, the CF positions shift shortwards with increasing temperatures. The RB1 position derived for each temperature are centered around 9.08-9.19 μm, the RB1 position shifts longwards, and the RB1 emissivity decreases with increasing temperatures (similar to other silicates studied). The RB1 spectral contrast increases with increasing temperatures with $\Delta\mu = 0.035$. The broad TF is centered around 12 μm for all temperatures. Unlike feldspars studied, for nepheline, the slope between 7 μm and the CF positions significantly increases with increasing temperatures.

5. Discussions

5.1 Spectral trends as a function of temperature

In order to understand the evolution of emissivity spectra of these powdered silicates at varying hermean surface temperatures in Fig. 4, the derived spectral parameters are plotted against their corresponding temperatures and are discussed below.

CF position vs temperature (Fig. 4a): At the lowest temperatures (100 °C; Fig. 4a), the CF position of emissivity spectra behaves relatively linearly with respect to their corresponding silica polymerization (Conel, 1969; Cooper et al., 2002; Logan et al., 1973). At 100 °C, forsterite has the CF positioned at the longest wavelengths (~8.94 μm), pyroxenes at intermediate wavelengths ranging from 8.13 μm to 8.43 μm (diopside > hypersthene > enstatite), and plagioclase at the shortest wavelengths ranging from 7.56 μm to 7.95 μm (anorthite > labradorite > andesine > microcline > oligoclase). At 100 °C, nepheline has the same CF position as enstatite. With the increase in temperature, the CF positions of forsterite, diopside, enstatite, andesine, microcline, and oligoclase only slight shifts shortwards. The CF

positions of hypersthene and nepheline significantly shift shortwards at 400 °C and 200 °C, respectively, and the CF positions of anorthite shift longwards with the increase in temperature. As a result, at 500 °C, enstatite and hypersthene, show the inverse effect in CF position (enstatite > hypersthene) compared to their corresponding CF positions at 100 °C. In addition, pyroxenes (enstatite, hypersthene), the feldspathoid (nepheline), and plagioclase (anorthite) display only small differences among their CF positions at 500 °C. Among the plagioclase feldspars, the CF position of labradorite shifts significantly shortwards compared to andesine, resulting in only small differences among their respective CF positions at temperatures larger than 200 °C. Our results underline the importance of understanding the shifts in CF positions in the emissivity spectra as a function of temperature for the accurate interpretation of orbital spectra to derive the mineralogy of the observed spectra.

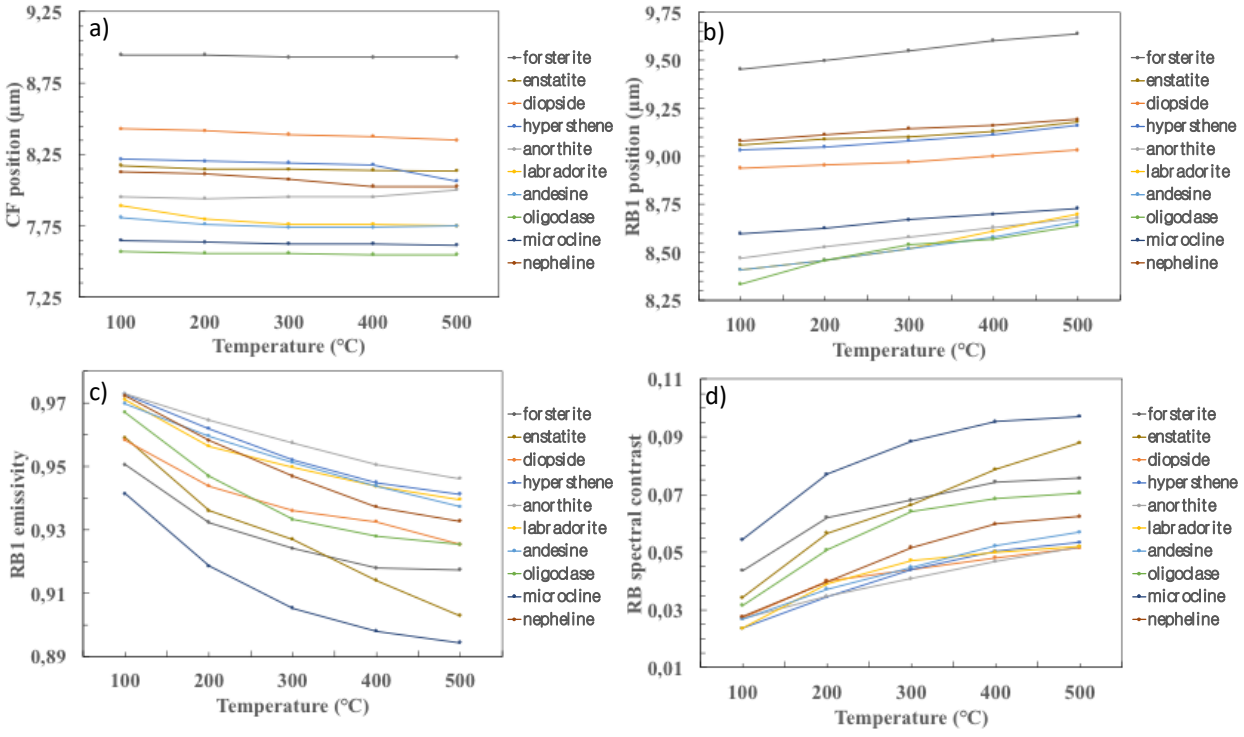

Figure 4. The derived spectral parameters; a) CF position (µm), b) RB1 position (µm), c) RB1 emissivity, and d) RB spectral contrast (µm) for each silicate are plotted against their corresponding sample temperature. The plot shows that a) the CF position does not vary significantly with increasing temperatures, b) the RB1 position increases with increasing temperatures and the major silicate groups are naturally clustered in the plot, c) the RB1 emissivity decreases with decreasing temperatures, and d) the RB spectral contrast increases with increasing temperatures.

RB1 position vs temperature (Fig. 4b): For all silicates, the RB1 positions of their emissivity spectra shift longwards with increasing temperatures (Fig. 4b) displaying positive slopes. Unlike CF positions, derived RB1 positions show that at all temperatures, forsterite, pyroxenes, and plagioclase feldspars can be uniquely identified depending on their corresponding RB1 positions, which fall within 9.45-9.64 μm, 8.41-9.45 μm, and 8.33-8.72 μm, respectively. However, the RB1 positions of the feldspathoid nepheline fall within the range of pyroxenes (8.41-9.45 μm).

RB1 emissivity vs temperature (Fig. 4c): For all silicates, the RB1 emissivity decreases with increasing temperatures in non-linear fashion (Fig. 4c). Unlike CF and RB1 positions, RB1 emissivities do not display specific correlations with regard to their silicate groups. However, our study suggests that the overall spectral contrast of emissivity spectra increases with increasing temperatures.

RB1 spectral contrast vs temperature (Fig. 4d): The RB1 spectral contrast defined by the slope between the emissivity at the CF position and the RB1 position, respectively, increases with increasing temperatures. This suggests that the strengths of the RBs increase with increasing temperatures. Like the RB1 emissivity, the RB1 spectral contrast does not uniquely identify different silicate groups. Although RB1 emissivity and RB1 spectral contrast do not help in uniquely identifying the silicate groups, their behavior as a function of temperature suggests the importance of creating a library of spectra obtained as a function of temperature for understanding the mineralogy of Mercury from the orbit.

5.2 Application to MERTIS data analysis

The absorption of certain frequencies in the infrared spectral region is directly due to the existence of specific atomic vibrations (Lane and Bishop, 2019; Salisbury et al., 1991; Salisbury et al., 1987). In the studied TIR spectral region, the spectral features of these silicate

minerals arise from the fundamental vibrational modes of the material (Salisbury et al., 1987). The primary spectral absorptions in the TIR spectral region (Reststrahlen bands) are due to the stretching and bending motions of the silicon–oxygen anions (Lane and Bishop, 2019). Additional absorption features result from metal–oxygen and lattice vibrations (Salisbury et al., 1991). Spectral features such as shapes, maxima or minima, and intensities are directly dependent on the relative masses, radii, and bond strengths and on structural arrangements in a crystal lattice. It follows that, since all minerals, by definition, have unique structures and/or compositions, virtually every mineral has a different suite of vibrational absorption characteristics and thus a unique spectrum in the thermal infrared (Hamilton, 2010).

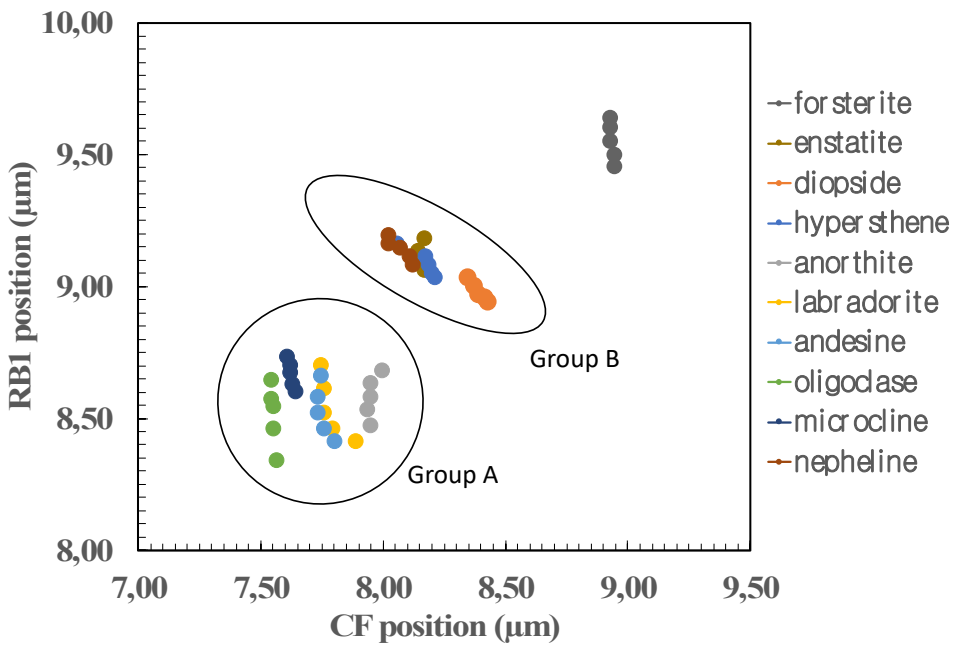

Figure 5. Plot between CF position and RB1 position (CF vs RB1 plot) showing that the three major silicate groups olivine (forsterite), pyroxenes (Group B), and feldspars (Group A) are naturally clustered into different groups and therefore can be unambiguously identified in TIR spectra irrespective of their cations and surface temperatures. The silica-undersaturated aluminosilicate, nepheline, falls into Group B. For all silicates, RB1 positions shift to longer wavelengths with increasing temperatures (100 °C to 500 °C). The data trend in the plot can be broadly interpreted as the datapoints shift from bottom-left to upper-right corner of the plot with decreasing amount of Si-O among the silicate minerals studied.

Among all the spectral parameters derived as a function of temperature, CF and RB1 positions give direct insight into the particular silicate group. Combined together, these two

parameters should enable unambiguous identification of these silicate groups from orbit and telescopic observations, irrespective of surface temperatures. In order to achieve this, in this study, we introduce the CF vs RB1 plot in Fig. 5.

Plagioclase feldspars (Group A), pyroxenes (Group B), and forsterite are naturally clustered into three different locations in the CF vs RB1 plot (Fig. 5), irrespective of the temperature. However, the nepheline (feldspathoid) datapoints fall within the pyroxene class (Group B).

Group A silicates (feldspars) show that with increasing temperatures their CF positions are not as strongly affected as their RB1 positions. But from Na-rich oligoclase to Ca-rich anorthite, the CF positions shifted longwards pointing to the possibility to distinguish even plagioclase phases in the TIR. Group B silicates (pyroxenes and nepheline) show that both CF and RB1 positions are affected with increasing temperatures. For this group, the CF positions shift shortwards and the RB1 positions shift longwards with increasing temperatures.

As forsterite is the only mineral studied among the olivine family, we did not define general boundaries as for Group A and Group B silicates. Forsterite shows that the CF position is least affected by the increase in temperature; however, the RB1 position increases longwards with increasing temperatures similar to Group A silicates.

The CF vs RB1 plot (Fig. 5) can be used to identify olivine, pyroxenes (and nepheline) (Group B), and plagioclase (Group A) silicates when comparing two spectral parameters instead of just one (CF position or RB1 position). This plot will further enable a quick first order surface mineral identification in MERTIS data and ground-based telescopic observations in the TIR spectral region. The data trend in the plot can be visualised as the datapoints shift from the lower-left to the upper-right corner with decreasing amounts of Si-O among the igneous silicate minerals studied.

6. Conclusions

This study investigated temperature-dependent emissivity spectra of powdered silicates measured under simulated daytime surface conditions of Mercury. These spectra will facilitate the high-resolution mineral mapping of Mercury's surface by the MERTIS instrument on the BepiColombo mission at spatial resolutions better than 500 m/pixel. By carefully investigating the derived spectral parameters, the study suggests that combined information from the CF and the RB1 band (CF vs RB1 plot) can uniquely distinguish major silicate groups and also depending on the Si-O content. MERTIS-derived global variations of the CF and the RB1 will facilitate the characterization of Mercury's surface mineralogy and igneous rock types. In addition, the CF vs RB1 plot can be applied beyond Mercury to map the surface mineralogy of various silicate targets such as the Moon, Mars, and S-type asteroids in the TIR spectral range from orbit or telescopic observations.

Acknowledgments

IV is thankful for receiving a DLR/DAAD Doctorate Fellowship for funding her PhD work at PSL-DLR. A portion of this research was supported by the European Union's Horizon 2020 research and innovation program. Europlanet 2020 RI has received funding from the European Union's Horizon 2020 research and innovation programme under grant agreement No 654208.

References

Armstrong, J.T., 1995. Citzaf-a package of correction programs for the quantitative Electron Microbeam X-Ray-Analysis of thick polished materials, thin-films, and particles. Microbeam Analysis 4, 177-200.

501 Besse, S., Doressoundiram, A., Benkhoff, J., 2015. Spectroscopic properties of explosive
502 volcanism within the Caloris basin with MESSENGER observations. Journal of
503 Geophysical Research: Planets 120, 2102-2117.

504 Blewett, D.T., Chabot, N.L., Denevi, B.W., Ernst, C.M., Head, J.W., Izenberg, N.R., Murchie,
505 S.L., Solomon, S.C., Nittler, L.R., McCoy, T.J., Xiao, Z., Baker, D.M.H., Fassett, C.I.,
506 Braden, S.E., Oberst, J., Scholten, F., Preusker, F., Hurwitz, D.M., 2011. Hollows on
507 Mercury: MESSENGER Evidence for Geologically Recent Volatile-Related Activity.
508 Science 333, 1856-1859.

509 Chihara, H., Koike, C., Tsuchiyama, A., 2001. Low-temperature optical properties of silicate
510 particles in the far-infrared region. Publications of the Astronomical Society of Japan
511 53, 243-250.

512 Christensen, P.R., Bandfield, J.L., Hamilton, V.E., Howard, D.A., Lane, M.D., Piatek, J.L.,
513 Ruff, S.W., Stefanov, W.L., 2000. A thermal emission spectral library of rock-forming
514 minerals. Journal of Geophysical Research: Planets 105, 9735-9739.

515 Conel, J.E., 1969. Infrared emissivities of silicates: Experimental results and a cloudy
516 atmosphere model of Spectral emission from condensed particulate mediums. Journal
517 of Geophysical Research (1896-1977) 74, 1614-1634.

518 Cooper, B.L., Salisbury, J.W., Killen, R.M., Potter, A.E., 2002. Midinfrared spectral features
519 of rocks and their powders. Journal of Geophysical Research: Planets 107, 1-1-1-17.

520 D'Amore, M., Helbert, J., Maturilli, A., Varatharajan, I., Ulmer, B., Säuberlich, T., Berlin, R.,
521 Peter, G., Hiesinger, H., Arnold, G., 2019. The mercury radiometer and thermal infrared

imaging spectrometer (MERTIS) onboard Bepi Colombo: first inflight calibration results. SPIE.

Deer, W.A., FRS, Howie, R.A., Zussman, J., 2013. An Introduction to the Rock-Forming Minerals. Mineralogical Society of Great Britain and Ireland.

Donaldson Hanna, K.L., Thomas, I.R., Bowles, N.E., Greenhagen, B.T., Pieters, C.M., Mustard, J.F., Jackson, C.R.M., Wyatt, M.B., 2012. Laboratory emissivity measurements of the plagioclase solid solution series under varying environmental conditions. Journal of Geophysical Research: Planets 117.

Ferrari, S., Maturilli, A., Carli, C., D'Amore, M., Helbert, J., Nestola, F., Hiesinger, H., 2020. Thermal infrared emissivity of felsic-rich to mafic-rich analogues of hot planetary regoliths. Earth and Planetary Science Letters 534, 116089.

Ferrari, S., Nestola, F., Massironi, M., Maturilli, A., Helbert, J., Alvaro, M., Domeneghetti, M.C., Zorzi, F., 2014. In-situ high-temperature emissivity spectra and thermal expansion of C2/c pyroxenes: Implications for the surface of Mercury. American Mineralogist 99, 786-792.

Goudge, T.A., Head, J.W., Kerber, L., Blewett, D.T., Denevi, B.W., Domingue, D.L., Gillis-Davis, J.J., Gwinner, K., Helbert, J., Holsclaw, G.M., Izenberg, N.R., Klima, R.L., McClintock, W.E., Murchie, S.L., Neumann, G.A., Smith, D.E., Strom, R.G., Xiao, Z., Zuber, M.T., Solomon, S.C., 2014. Global inventory and characterization of pyroclastic deposits on Mercury: New insights into pyroclastic activity from MESSENGER orbital data. Journal of Geophysical Research E: Planets 119, 635-658.

543 Hamilton, V.E., 2000. Thermal infrared emission spectroscopy of the pyroxene mineral series.
544 Journal of Geophysical Research: Planets 105, 9701-9716.

545 Hamilton, V.E., 2010. Thermal infrared (vibrational) spectroscopy of Mg–Fe olivines: A
546 review and applications to determining the composition of planetary surfaces.
547 Geochemistry 70, 7-33.

548 Hapke, B., 2012. Theory of Reflectance and Emittance Spectroscopy, 2 ed. Cambridge
549 University Press, Cambridge.

550 Helbert, J., Hiesinger, H., Walter, I., Säuberlich, T., Maturilli, A., D'Amore, M., Knollenberg,
551 J., Lorenz, E., Peter, G., Arnold, G., 2010. MERTIS: understanding Mercury's surface
552 composition from mid-infrared spectroscopy. SPIE.

553 Helbert, J., Maturilli, A., 2009. The emissivity of a fine-grained labradorite sample at typical
554 Mercury dayside temperatures. Earth and Planetary Science Letters 285, 347-354.

555 Helbert, J., Maturilli, A., D'Amore, M., 2013a. Visible and near-infrared reflectance spectra of
556 thermally processed synthetic sulfides as a potential analog for the hollow forming
557 materials on Mercury. Earth and Planetary Science Letters 369–370, 233-238.

558 Helbert, J., Moroz, L.V., Maturilli, A., Bischoff, A., Warell, J., Sprague, A., Palomba, E., 2007.
559 A set of laboratory analogue materials for the MERTIS instrument on the ESA
560 BepiColombo mission to Mercury. Advances in Space Research 40, 272-279.

561 Helbert, J., Nestola, F., Ferrari, S., Maturilli, A., Massironi, M., Redhammer, G.J., Capria,
562 M.T., Carli, C., Capaccioni, F., Bruno, M., 2013b. Olivine thermal emissivity under

563 extreme temperature ranges: Implication for Mercury surface. Earth and Planetary
564 Science Letters 371, 252-257.

565 Hiesinger, H., Helbert, J., Alemanno, G., Bauch, K.E., D'Amore, M., Maturilli, A., Morlok, A.,
566 Reitze, M.P., Stangarone, C., Stojic, A.N., Varatharajan, I., Weber, I., the, M.C.-I.T.,
567 2020. Studying the Composition and Mineralogy of the Hermean Surface with the
568 Mercury Radiometer and Thermal Infrared Spectrometer (MERTIS) for the
569 BepiColombo Mission: An Update. Space Science Reviews 216, 110.

570 Hiesinger, H., Helbert, J., MERTIS Co-I Team, 2010. The Mercury Radiometer and Thermal
571 Infrared Spectrometer (MERTIS) for the BepiColombo mission. Planetary and Space
572 Science 58, 144-165.

573 Izenberg, N.R., Klima, R.L., Murchie, S.L., Blewett, D.T., Holsclaw, G.M., McClintock, W.E.,
574 Malaret, E., Mauceri, C., Vilas, F., Sprague, A.L., Helbert, J., Domingue, D.L., Head
575 Iii, J.W., Goudge, T.A., Solomon, S.C., Hibbitts, C.A., Dyar, M.D., 2014. The low-iron,
576 reduced surface of Mercury as seen in spectral reflectance by MESSENGER. Icarus
577 228, 364-374.

578 Koike, C., Chihara, H., Tsuchiyama, A., Suto, H., Sogawa, H., Okuda, H., 2003. Compositional
579 dependence of infrared absorption spectra of crystalline silicate. A&A 399, 1101-1107.

580 Koike, C., Mutschke, H., Suto, H., Naoi, T., Chihara, H., Henning, T., Jäger, C., Tsuchiyama,
581 A., Dorschner, J., Okuda, H., 2006. Temperature effects on the mid-and far-infrared
582 spectra of olivine particles. A&A 449, 583-596.

583 Krotikov, V.D., Shchuko, O.B., 1975. Thermal conditions in the surface layer of Mercury.
584 Astronomicheskii Zhurnal 52, 146.

585 Lane, M.D., Bishop, J.L., 2019. Mid-infrared (Thermal) Emission and Reflectance
586 Spectroscopy: Laboratory Spectra of Geologic Materials, in: Bell Iii, J.F., Bishop, J.L.,
587 Moersch, J.E. (Eds.), Remote Compositional Analysis: Techniques for Understanding
588 Spectroscopy, Mineralogy, and Geochemistry of Planetary Surfaces. Cambridge
589 University Press, Cambridge, pp. 42-67.

590 Logan, L.M., Hunt, G.R., Salisbury, J.W., Balsamo, S.R., 1973. Compositional implications of
591 Christiansen frequency maximums for infrared remote sensing applications. Journal of
592 Geophysical Research (1896-1977) 78, 4983-5003.

593 Lyon, R.J.P., 1965. Analysis of rocks by spectral infrared emission (8 to 25 microns). Economic
594 Geology 60, 715-736.

595 Maturilli, A., Donaldson Hanna, K.L., Helbert, J.r., Pieters, C., 2013. A New Standard for
596 Calibration of High Temperature Emissivity: Laboratory Intercalibration at PEL of
597 DLR and ALEC of Brown University, LPSC 2013.

598 Maturilli, A., Helbert, J., Amore, M.D., Varatharajan, I., Hiesinger, H., Bauch, K., 2018a. The
599 operations plan for the MErcury Radiometer and Thermal infrared Imaging
600 Spectrometer (MERTIS) on its way to Mercury. SPIE.

601 Maturilli, A., Helbert, J., Amore, M.D., Varatharajan, I., Ortiz, Y.R., 2018b. The Planetary
602 Spectroscopy Laboratory (PSL): wide spectral range, wider sample temperature range.
603 SPIE.

Maturilli, A., Helbert, J., St. John, J.M., Head Iii, J.W., Vaughan, W.M., D'Amore, M., Gottschalk, M., Ferrari, S., 2014. Komatiites as Mercury surface analogues: Spectral measurements at PEL. Earth and Planetary Science Letters 398, 58-65.

Maturilli, A., Helbert, J., Varatharajan, I., 2019. Graphite as Potential Darkening Agent for Mercury: Spectral Measurements Under Simulated Mercury Conditions, Lunar and Planetary Science Conference.

Morimoto, N., 1988. Nomenclature of Pyroxenes. Mineralogy and Petrology 39, 55-76.

Namur, O., Charlier, B., 2017. Silicate mineralogy at the surface of Mercury. Nature Geosci 10, 9-13.

Reitze, M., Morlok, A., Hiesinger, H., Weber, I., Stojic, A., 2017. Infrared spectroscopy of Mercury analogue materials under simulated Mercury surface temperature conditions, p. 17491.

Reitze, M.P., Weber, I., Kroll, H., Morlok, A., Hiesinger, H., Helbert, J., 2020. Mid-infrared spectroscopy of alkali feldspar samples for space application. Mineralogy and Petrology 114, 453-463.

Salisbury, J.W., D'Aria, D.M., Jarosewich, E., 1991. Midinfrared (2.5–13.5 μm) reflectance spectra of powdered stony meteorites. Icarus 92, 280-297.

Salisbury, J.W., Walter, L.S., Vergo, N., D'Aria, D., 1987. Mid-infrared (2.1-25 μm) snectra of minerals. U.S. Geological Survey Open File Report 87-263. Reston.

623 Shevchenko, V.V., 2002. The Structure of the Surface of Mercury's Regolith from Remote
624 Sensing Data. Solar System Research 36, 359-366.

625 Sprague, A.L., Donaldson Hanna, K.L., Kozlowski, R.W.H., Helbert, J., Maturilli, A., Warell,
626 J.B., Hora, J.L., 2009. Spectral emissivity measurements of Mercury's surface indicate
627 Mg- and Ca-rich mineralogy, K-spar, Na-rich plagioclase, rutile, with possible
628 perovskite, and garnet. Planetary and Space Science 57, 364-383.

629 Stangarone, C., 2017. Ab initio calculations of Raman and IR spectra of orthoenstatite and
630 forsterite: lattice dynamics and modelling for planetary remote sensing. Universita'degli
631 studi di Parma. Dipartimento di Fisica e Scienze della ….

632 Stangarone, C., Helbert, J., Maturilli, A., Tribaudino, M., Prencipe, M., 2017. Modelling of
633 thermal-IR spectra of forsterite: application on remote sensing for Mercury. European
634 Planetary Science Congress 11.

635 Vander Kaaden, K.E., M. McCubbin, F., R. Nittler, L., N. Peplowski, P., Z. Weider, S., A.
636 Frank, E., J. McCoy, T., 2017. Geochemistry, mineralogy, and petrology of boninitic
637 and komatiitic rocks on the mercurian surface: Insights into the mercurian mantle. Icarus
638 285, 155-168.

639 Varatharajan, I., D'Amore, M., Maturilli, A., Helbert, J., Hiesinger, H., 2018. Machine Learning
640 Approach to Deconvolution of Mid-Infrared Telescope Spectra of Mercury: Supporting
641 MERTIS onboard ESA/JAXA BepiColombo mission, AGU Fall Meeting Abstracts, pp.
642 P41D-3762.

643 Varatharajan, I., Maturilli, A., Helbert, J., Alemanno, G., Hiesinger, H., 2019. Spectral behavior
644 of sulfides in simulated daytime surface conditions of Mercury: Supporting past
645 (MESSENGER) and future missions (BepiColombo). Earth and Planetary Science
646 Letters 520, 127-140.

647 Vilas, F., Domingue, D.L., Helbert, J., D'Amore, M., Maturilli, A., Klima, R.L., Stockstill-
648 Cahill, K.R., Murchie, S.L., Izenberg, N.R., Blewett, D.T., Vaughan, W.M., Head, J.W.,
649 2016. Mineralogical indicators of Mercury's hollows composition in MESSENGER
650 color observations. Geophysical Research Letters 43, 1450-1456.

651

652